Bone 43 (2008) 302–311

Contents lists available at ScienceDirect

Bone

journal homepage: www.elsevier.com/locate/bone

Quantitative micro-computed tomography: A non-invasive method to assess equivalent bone mineral density

Ara Nazarian [a,c], Brian D. Snyder [a,b], David Zurakowski [b], Ralph Müller [c,d,*]

[a] Orthopedic Biomechanics Laboratory, Beth Israel Deaconess Medical Center and Harvard Medical School, Boston, MA, 02215, USA
[b] Department of Orthopaedic Surgery, Children's Hospital, Harvard Medical School, Boston, MA 02115, USA
[c] Institute for Biomedical Engineering, University and ETH Zürich, 8044 Zürich, Switzerland
[d] Institute for Biomechanics, ETH Zürich, 8093 Zürich, Switzerland

ARTICLE INFO

Article history:
Received 23 May 2007
Revised 10 April 2008
Accepted 14 April 2008
Available online 30 April 2008

Edited by: Harry Genant

Keywords:
Micro-computed tomography
Calibration phantom
Calibration
Bone density
Bone mineralization

ABSTRACT

One of the many applications of micro computed tomography (μCT) is to accurately visualize and quantify cancellous bone microstructure. However, μCT based assessment of bone mineral density has yet to be thoroughly investigated. Specifically, the effects of varying imaging parameters, such as tube voltage (kVp), current (μA), integration time (ms), object to X-ray source distance (mm), projection number, detector array size and imaging media (surrounding the specimen), on the relationship between equivalent tissue density (ρ_{EQ}) and its linear attenuation coefficient (μ) have received little attention. In this study, in house manufactured, hydrogen dipotassium phosphate liquid calibration phantoms (K_2HPO_4) were employed in addition to a resin embedded hydroxyapatite solid calibration phantoms supplied by Scanco Medical AG Company. Variations in current, integration time and projection number had no effect on the conversion relationship between μ and ρ_{EQ} for the K_2HPO_4 and Scanco calibration phantoms [$p>0.05$ for all cases]. However, as expected, variations in scanning tube voltage, object to X-ray source distance, detector array size and imaging media (referring to the solution that surrounds the specimen in the imaging vial) significantly affected the conversion relationship between μ and ρ_{EQ} for K_2HPO_4 and Scanco calibration phantoms [$p<0.05$ for all cases]. A multivariate linear regression approach was used to estimate ρ_{EQ} based on attenuation coefficient, tube voltage, object to X-ray source distance, detector array size and imaging media for K_2HPO_4 liquid calibration phantoms, explaining 90% of the variation in ρ_{EQ}. Furthermore, equivalent density values of bovine cortical bone (converted from attenuation coefficient to equivalent density using the K_2HPO_4 liquid calibration phantoms) samples highly correlated [$R^2=0.92$] with the ash densities of the samples.

In conclusion, Scanco calibration phantoms can be used to assess equivalent bone mineral density; however, they cannot be scanned with a specimen or submerged in a different imaging media. The K_2HPO_4 liquid calibration phantoms provide a cost effective, easy to prepare and convenient means to perform quantitative μCT analysis using any μCT system, with the ability to choose different imaging media according to study needs. However, as with any liquid calibration phantom, they are susceptible to degradation over time.

Introduction

Micro-computed tomography (μCT) has been used extensively to generate high-resolution images of cancellous and cortical bone morphology from normal and pathologic human and animal specimens [1,2]. While μCT has effectively become the standard tool to quantify bone morphology and microstructure, little headway has been made in establishing μCT as a tool to provide quantitative mineralization assessment of calcified tissue. Currently available methods of dual energy X-ray absorptiometry (DXA) [3–6] and quantitative computed tomography (QCT) [7] provide insufficient resolution to investigate variations of mineralization in cancellous bone, whereas backscattered electron microscopy (BSE) provides a high resolution but destructive and two-dimensional account of the three-dimensional calcified tissue mineralization [8–10]. Synchrotron radiation computed tomography, despite generating non-destructive (specimen) and extremely high resolution images with monochromatic X-ray beams, is available on a very limited basis and only for relatively small specimens [11].

At present, μCT generated images are used to quantify the effects of pathologic and pharmacological manipulations on bone microstructure. However, little information can be extracted from these images to quantify the potential effects of these manipulations on bone material properties. Moreover, μCT images are used to generate

* Corresponding author. Institute for Biomechanics, ETH Zürich, HCI E357.2, Wolfgang-Pauli-Strasse 10, 8093 Zürich, Switzerland. Fax: +41 1 632 1214.
E-mail address: ram@ethz.ch (R. Müller).

8756-3282/$ – see front matter © 2008 Elsevier Inc. All rights reserved.
doi:10.1016/j.bone.2008.04.009

structural models for finite element analysis (FEA) of various trabecular microstructures, but a localized material profile of the bone tissue is difficult to establish, often forcing researchers to assign homogeneous material properties to study a decidedly non-homogeneous material.

On the other hand, clinical computed tomography systems, in conjunction with calibration phantoms to mimic the attenuation of various tissue types [12–14], have been used successfully as a diagnostic tool in many medical disciplines [15–18]. For instance, calibration phantoms have been devised to quantify bone mineral density from CT images [19–26], as Witt and Cameron invented the K_2HPO_4 liquid calibration phantoms [27], and Cann and Genant used this type of liquid calibration phantom in the 1980s to measure vertebral mineral content [28].

While the use of these calibration phantoms has become commonplace in clinical settings, the technical and physical factors that influence the analytic relationship for converting X-ray attenuation coefficients (μ, cm^{-1}) to equivalent bone mineral density (ρ_{EQ}, g cm^{-3}) have not been fully studied for research-based high resolution μCT imaging. Algorithms that correct for polychromatic beam hardening have significantly improved upon an important technical obstacle affecting the linearity of the relationship between bone mineral density and attenuation coefficient measured by μCT. Yet, the effects of varying the X-ray source tube voltage (kVp), current (μA), integration time (ms), object to X-ray source distance (mm), projection number, detector array size, and imaging media (surrounding the specimen) on the relationship between equivalent tissue density and its linear attenuation coefficient have received little attention. The effects of μCT scanning parameters on the measured linear attenuation are important from both practical and physical points of view. Practically speaking, specimens are scanned at different scan settings at labs for a variety of reasons, and operators can only change scanning parameters available on the system, most commonly tube voltage, current, object to X-ray source distance (secondarily as voxel size and imaging vial diameter), integration time, projections number, detector size and imaging media. From a physical standpoint, a change in each of these parameters can result in changes in the measured attenuation of the specimen mineral content. For instance, tube voltage has an inverse relationship with the measured linear attenuation, and increased tube current and integration time (the shutter stays open longer) should result in reduced image noise, as this reduction can facilitate the use of smaller tube voltage

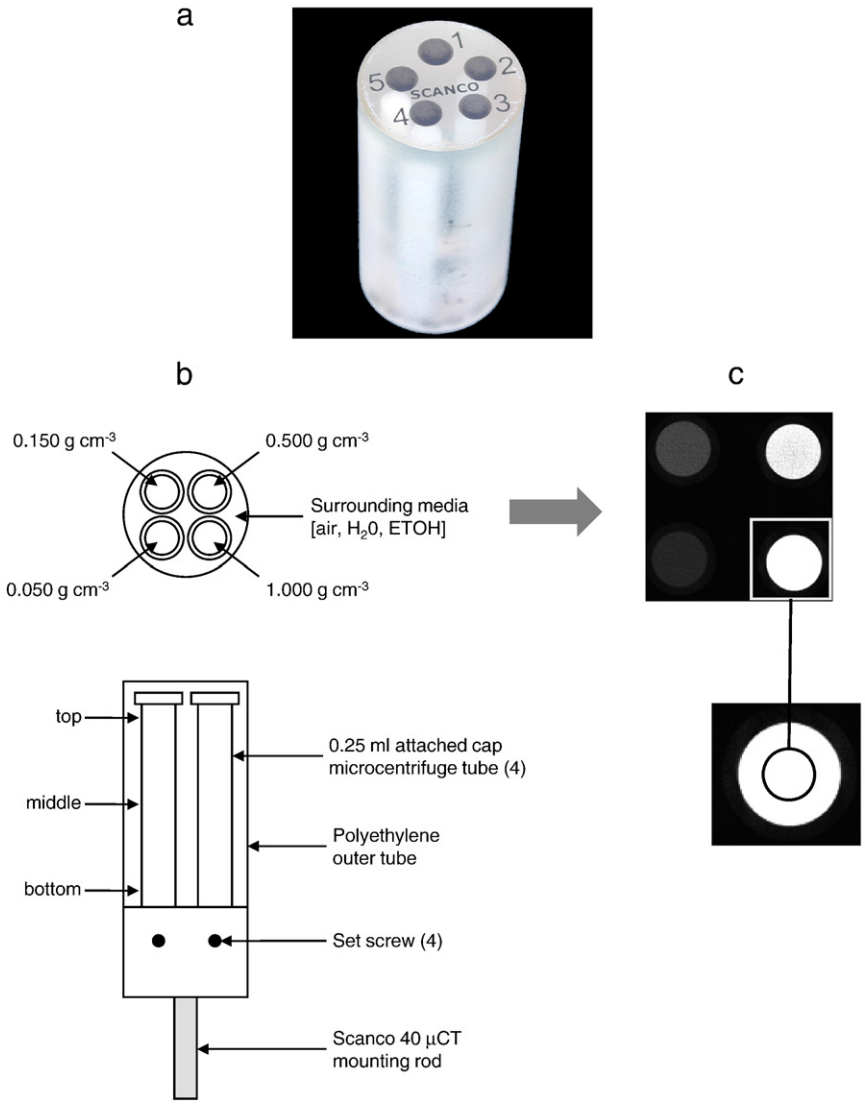

Fig. 1. An image of the Scanco HA solid phantom, b: Schematic diagram of the K_2HPO_4 liquid calibration phantom, c: a representative μCT slice of the K_2HPO_4 calibration phantom with the evaluation contour (half the diameter of the calibration phantom) shown with black circle in the image callout.

Table 1
Comparison of atomic number, X-ray attenuation coefficient and equivalent density derived from X-ray attenuation properties for HA, K_2HPO_4 and $K_4P_2O_7$ for use as bone mineral density phantoms

Property	Unit	HA	K_2HPO_4	$K_4P_2O_7$	HA–K_2HPO_4 Difference (%)	HA–$K_4P_2O_7$ Difference (%)
Effective atomic number	–	15.86	15.58	15.87	1.77	− 0.06
Density	g cm^{-3}	1.161	1.144	1.155	1.46	0.52
X-ray attenuation at 40keV	(cm^{-1})	4.131	4.027	4.092	2.52	0.94
at 60keV	(cm^{-1})	2.642	2.582	2.603	2.27	1.48
At 80keV	(cm^{-1})	2.201	2.152	2.163	2.23	1.73

without significant loss in image quality and reproducibility [29]. This experimental study evaluates these factors affecting the X-ray attenuation of calcified tissue in order to present a reference point for those interested in μCT-based quantification of calcified tissue mineralization.

To this aim, our objectives were to establish a technique to measure the equivalent bone mineral density using a calibration phantom; to investigate the effects of physical and technical constraints on the conversion relationship between X-ray attenuation coefficient and bone mineral tissue density; and to validate the μCT calibration phantom-based equivalent bone mineral density with directly measured ash density.

Methods

Calibration phantom preparations

Scanco Medical (Scanco Medical AG, Bassersdorf, Switzerland), the manufacturer of the μCT system, introduced its solid calibration phantoms manufactured based on the European spine and forearm calibration phantoms (Fig. 1a) [30,31]. The Scanco solid calibration phantoms (HA-SCANCO) consist of different concentrations of HA ($Ca_5(PO_4)_3OH$) crystals embedded in epoxy resin to mimic surrounding soft tissue (hence not to be imaged with any other imaging media) and are fitted with a bracket for direct mounting onto the scanner. The overall HA densities of the HA-SCANCO calibration phantoms are 0.000 (resin only), 0.099, 0.199, 0.399, and 0.800 g cm^{-3} of Ha corresponding to bone equivalent densities of 1.14, 1.20, 1.26, 1.38, and 1.62 g cm^{-3} respectively. Hydrogen dipotassium phosphate (K_2HPO_4) calibration phantoms of 0.050, 0.150, 0.500 and 1.000g cm^{-3} densities (Sigma-Aldrich, Steinheim, Switzerland) were used as the *liquid* calibration phantoms in this study [27,32]. K_2HPO_4 was selected due to the similarity of its previously mentioned properties to those of HA (Table 1).

Other compounds, such as potassium pyrophosphate ($K_4P_2O_7$), also have similar properties to HA, yet their application as bone calibration phantoms has not been as extensive as that of K_2HPO_4 [33]. The liquid calibration phantom solutions were prepared in sterile glassware using 18.2MΩ double distilled water (Millipore,) and were filled and capped in a sterile environment to avoid introduction of foreign particles to the solutions. The liquids were filled in 0.25ml microcentrifuge plastic tubes with attached caps (Fisher Scientific, Pittsburgh, PA), until a positive meniscus was formed at the top of the tube. Each tube was then capped and sealed with epoxy glue to avoid introduction of air bubbles inside the vial and/or calibration phantom fluid leakage.

A cylinder shaped fixture (∅: 20.50 mm, H: 20.00 mm) was designed with four equidistant holes (∅: 5.40 mm) to accommodate four calibration phantom vials. The holes were equally spaced at 90° from one another and were placed in a circular pattern with a diameter of 11.50 mm, to ensure equal exposure of all vials to the X-ray beam. In order to prevent the calibration phantom vials from rotating in the fixture, a small non-metallic set screw was used to hold each calibration phantom vial in a fixed position at all times (Fig. 1b). Solid hydroxyapatite calibration phantoms, commonly used for clinical applications, present with a heterogeneous distribution of mineral crystal embedded in resin, contributing to larger variation in linear attenuation. On the other hand, K_2HPO_4 liquid calibration phantoms are similar in atomic weight and X-ray attenuation to hydroxyapatite but are soluble and therefore much more homogeneous at the microscopic level. However, as with any liquid calibration phantom, they are subject to leaching and formation of air bubbles after a period of time.

μCT imaging and analysis

A 1.8 mm *trans*-axial segment was imaged three times at an isotropic voxel size of 20 μm through each calibration phantom using a Scanco μCT40 (Scanco Medical AG, Bassersdorf, Switzerland) imaging system. This system consists of an X-ray tube capable of producing cone beams detected by a CCD detector with 2048×256 detectors (2048×2048 pixels per cross section) [34]. Image cross sections were reconstructed using the manufacturer's cone beam reconstruction algorithm, following the general principles of the Feldkamp cone beam reconstruction. The X-ray beam was filtered with a 0.5 mm aluminum filter for a modified X-ray exit spectrum, and polychromatic beam hardening corrections were employed during the reconstruction process by applying polynomial correction terms especially designed for cancellous bone (all according to manufacturer's guidelines).

Prior to undertaking this study, the μCT attenuation field uniformity was examined. Thirty five attenuation coefficient value were sampled from the center going outward in a concentric fashion using a water filled vial scanned at 70kVp, 114 μA, 250 ms, and 0.020 mm isotropic voxel size to assess the field uniformity. The results indicated that field uniformity was found to be within 0.65% across a 20 mm dial vial filled with water only.

The calibration phantoms were imaged with imaging media other than air (saline or ethyl alcohol (ETOH)) without the need to remove the air from the vials via vacuum pumping, as no air bubbles were observed in the images. Removal of air from μCT imaging vials is not a routine practice at labs that regularly perform this type of imaging and analysis

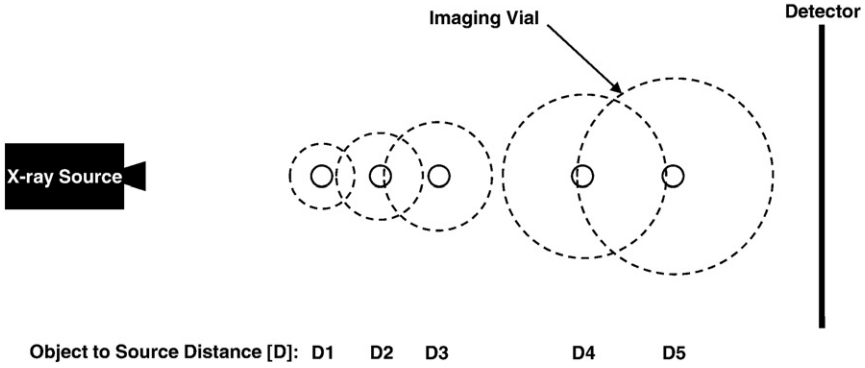

Fig. 2. Schematic diagram to illustrate the interplay between object size, object to X-ray source distance and detector array size. Scanco settings have 5 "diameter" settings (12.3, 16.4, 20.5, 30.7, 36.9 mm), referring to 5 different sizes of scanning vials. For instance, an object can be scanned in the 20.5 mm "diameter" vial with STANDARD "resolution" setting (meaning a detector array size of 1024×1024 and 250 projections/180°) resulting in an image with 20 μm isotropic voxel size. The same object can be scanned in the same vial with HIGH "resolution" setting (meaning a detector array size of 2048×2048 and 1000 projections/180°) for an image with 10 μm isotropic voxel size. In the abovementioned scenario, the object to X-ray source distances were identical in both cases, and only the detector array size and number of projections were modified. However, the same object can be scanned under STANDARD "resolution" setting in a larger vial (30.7 mm), which will have the same detector array size and projection number as the former, yet it will result in an image with 30 μm isotropic voxel size, since the object to X-ray source distance will be different. The distances given in this schematic are approximate and only serve to highlight the relative location of the object to the X-ray source during different imaging settings.

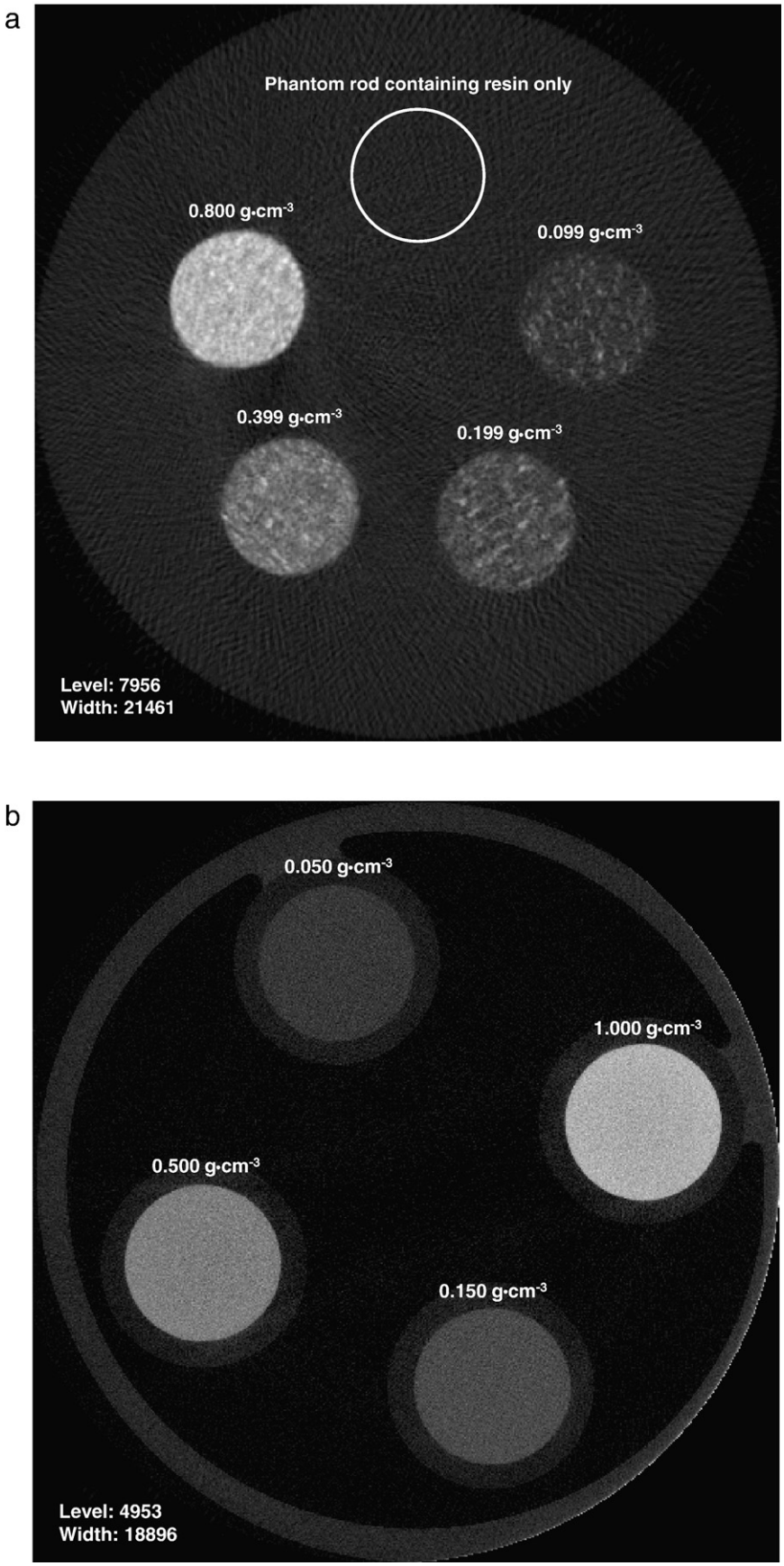

Fig. 3. Representative slices of the HA-SCANCO (a) and K_2HPO_4 (b) calibration phantoms, scanned under identical settings (70 kVp tube voltage, 114 μA current, 250 ms integration time and 15 μm pixel size).

on skeletal tissue. A circular region of interest (ROI) with half the diameter of each calibration phantom cross-section, placed at the center of the calibration phantom image (where the effects of beam hardening were at minimum), was contoured for calculating the X-ray attenuation coefficient throughout the study (Fig. 1c).

Study design and analysis

A default scanning parameter was chosen for the study: tube voltage: 70 kVp, beam current: 0.114 mA, pixel size: 30 μm, imaging media: air and integration time: 250 ms.

Intra-phantom homogeneity and spatial variation of the linear X-ray attenuation coefficient was investigated by imaging through the top, middle and bottom (Fig. 1b) of the HA-SCANCO and K_2HPO_4 calibration phantoms using default scanning parameters. Serial μCT scans obtained weekly, with identical scanning parameters, over a three-month period tested the variation of the X-ray attenuation coefficients for the HA-SCANCO and K_2HPO_4 calibration phantoms over time. Scanner drift was recorded at the duration of this study (it is a common practice at this laboratory to maintain a scanner drift log by scanning a solid calibration phantom (calibration phantom with little or no change in composition over time) at a regular time interval (once a month). One-way analysis of covariance (ANCOVA) was performed to test the effects of spatial variation and time on the slope of the fitted relationship between μ and ρ_{EQ}. If time or location was not significant, it was removed from the model to obtain a fitted linear equation of the form $\rho_{EQ}=a\cdot\mu+b$ (where a and b are constants).

Inter-scan variability was assessed by observing the average calibration phantom X-ray attenuation coefficient standard deviation of three identical scans, whereas intra-scan variation was assessed as the variation of X-ray attenuation coefficient within one scan at each concentration and calibration phantom type.

Using the calibration phantom as a surrogate for bone, parametric analyses were performed to evaluate the effects of varying scanning tube voltage, current, integration time, object to X-ray source distance, projection number, detector array size, and surrounding imaging media on the X-ray attenuation coefficient of K_2HPO_4 and HA-SCANCO calibration phantoms. This study was conducted using a Scanco μCT40 system with specific control settings for each parameter, however, the principals behind the study hold true for any scanner. The tube voltage (E) settings consist of 45, 55 and 70 kVp (the settings available to users by manufacturer and used extensively in the field), while the current (I) has low (I_{LOW}) and high (I_{HIGH}) settings for each tube voltage level (for E=70kVp, I_{LOW}=57 and I_{HIGH}=114μA | for E=55kVp, I_{LOW}=72 and I_{HIGH}=145μA | for E=45kVp, I_{LOW}=88 and I_{HIGH}=177μA). Integration time (t_{INT}) settings are chosen to be 60, 100, 200 and 250 ms, as these values represent t_{INT} values employed predominantly in musculoskeletal studies. The pixel size is a function of the size of the object, the distance the object is placed from the X-ray source, and the detector array size. The object to be imaged is placed in a vial, where 4 "diameter" settings (12.3, 16.4, 20.5, 30.7 and 36.9 mm) are used in the Scanco 40 system, and the "resolution" setting has three options of standard, medium and high, which is a function of detector array size and projection numbers per 180°.

From a physical stand point, the variation of the distance from the center of the vial (object) to the X-ray source (D) is the physical phenomena affecting the attenuation of the calibration phantom, where D settings of 3 (~ 55 mm) and 4 (~ 82 mm) were examined in this study (highly used settings) (Fig. 2). Additionally, two detector array size settings (DET) and three projection number settings (PN) were used as defined by the Scanco μCT40 system's *standard* (DET: 1024×1024, PN: 250), *medium* (DET: 1024×1024, PN: 500), and *high* (DET: 2048×2048, PN: 1000) "resolution" settings.

In musculoskeletal research, bone samples are imaged in an imaging media to mimic the presence of surrounding soft tissue (alcohol and saline as fat and muscle simulators respectively), for practical reasons such as keeping the specimen moist and/or preserved and/or for beam hardening corrections. Therefore, the K_2HPO_4 calibration phantoms were scanned either in air, saline or ethyl alcohol as the imaging media (MED) of choice. The calibration phantom holder was placed at the same location for all scans, as the holder sits on a block physically to ensure imaging of the same volume in space at all times. Additionally, the same reference line was used in the scout view to ensure imaging of the same calibration phantom region.

Two-way analysis of variance (ANOVA) was utilized to determine the effects of tube voltage, current, integration time, object to X-ray source distance, and imaging media (K_2HPO_4 calibration phantoms only) on μ for all equivalent densities and variables. Additionally, three-way factorial general linear analysis of variance (ANOVA) was used to assess the effect of detector size on attenuation. The model was a partially hierarchical design to account for the nesting effect of projection number within detector size. For each case, the equivalent density and the specific parameter in question (e.g. 45, 55 and 70 kVp tube voltage variation) was treated as fixed factors with μ as the dependent variable [35]. A general linear modeling approach was applied to determine the predictive information represented by μ and tube voltage alone and μ, tube voltage, object to X-ray source distance, detector array size, projection number, and imaging media in estimating equivalent density. The F-test was used to assess the significance of the predictive variables, and R^2 (coefficient of determination) was chosen as the criterion for summarizing the predictive accuracy of the fitted model [36].

In order to validate the μCT calibration phantom-based equivalent bone mineral density with directly measured ash density, twenty-one similarly sized cubes of bovine cortical bone (average side dimension and bone mass 6.03 mm±0.25 and 0.467 g±.016) were cut, weighed and randomly assigned to groups of 3 cubes each and were decalcified in ethylenediaminetetraacetic acid (EDTA) for 0, 2, 4, 6, 8, 10 or 12 days respectively to obtain bone samples covering a wide range of mineral content. Bone mineral density was derived using the K_2HPO_4 calibration phantom relationship to convert X-ray attenuation coefficient to an equivalent mineral density. The specimens were then dried in air and ashed (Furnace 48000, Thermolyne, Dubuque, Iowa) to determine the true mineral ash density ($\rho_{ASH}=m_{ASH}/V$) and ash content ($C_{ASH}=m_{ASH}/m_{DRY}$). The μCT derived bone mineral density, measured non-invasively, was compared to true mineral ash density for each specimen. The Bland–Altman method with 95% limits of agreement was used to assess the agreement between calibration phantom-derived equivalent density and ash density measured in the same samples. Two-tailed values of $p<0.05$ were considered statistically significant with a Bonferroni correction for multiple comparisons where appropriate. Data analysis was performed with the SPSS statistical package (version 14.0, SPSS Inc., Chicago, IL).

Results

The HA-SCANCO calibration phantoms showed much smaller intra-scan variations in μ across all concentrations (1.30%, 1.28%, 0.92% and 0.57% for 0.099, 0.199, 0.399 and 0.800g cm^{-3} calibration phantom densities) (Fig. 3a). Additionally, inter-scan variations for the same calibration phantoms imaged at the same location using the same imaging parameters resulted in variations of 0.05%, 0.04%, 0.09% and 0.06% (Table 2).

The K_2HPO_4 calibration phantoms revealed the least amount of intra-scan variation in μ across all concentrations (0.15%, 0.12%, 0.11% and 0.12% for 0.050, 0.150, 0.500 and 1.000g cm^{-3} calibration phantom densities) (Fig. 3b). Likewise, inter-scan variations for the same calibration phantoms imaged at identical location and conditions resulted in variations of 0.08%, 0.08%, 0.11% and 0.12% (Table 2).

The K_2HPO_4 and HA-SCANCO calibration phantom equivalent densities were homogeneous throughout the vials [K_2HPO_4: $p=0.37$ | HA-SCANCO: $p=0.28$], and the relationship between the K_2HPO_4 μ and ρ_{EQ} was unaffected by time over three months of observation (Fig. 4) [$p>0.99$ for all post-hoc comparisons]. Variations in current

Table 2
Average linear attenuation coefficients plus the standard deviation (in parenthesis) and coefficient of variation of all the concentrations of the Scanco HA and liquid K_2HPO_4 phantoms [all phantoms scanned at 70kVp tube voltage, 114μA current and 250ms integration time]

		Phantom concentration (g cm^{-3})			
Phantom	Type	0.050	0.150	0.500	1.000
K_2HPO_4 (cm^{-1})	Intra-scan variation	1.303 (.0012)	1.843 (.0015)	3.234 (.0027)	4.466 (.0035)
Coefficient of variation (%)		0.138	0.125	0.138	0.127
K_2HPO_4 (cm^{-1})	Inter-scan variation	1.317 (.0007)	1.835 (.0009)	3.199 (.0012)	4.474 (.0021)
Coefficient of variation (%)		0.080	0.081	0.061	0.086
		Phantom concentration (g cm^{-3})			
Phantom	Type	0.099	0.199	0.399	0.800
HA-SCANCO (SD (cm^{-1}))	Intra-scan variation	1.269 (0.014)	1.771 (0.019)	2.720 (0.019)	4.416 (0.018)
Coefficient of variation (%)		1.302	1.317	0.885	0.538
HA-SCANCO (SD) (cm^{-1})	Inter-scan variation	1.275 (0.0005)	1.778 (0.0006)	2.733 (0.0021)	4.439 (0.0022)
Coefficient of variation (%)		0.053	0.045	0.098	0.067

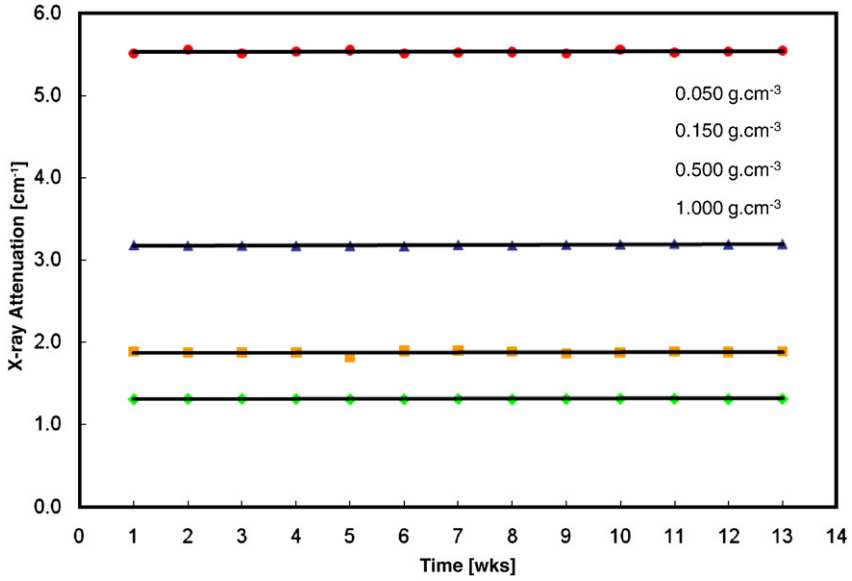

Fig. 4. Relationship between the measured K_2HPO_4 calibration phantom attenuations and time are demonstrated in this graph. The horizontal lines ($m=0$) illustrate the stability of the concentration data points in time. The standard deviation bars for all concentrations are too small to be seen in this figure.

[K_2HPO_4: $p=0.12$ | HA-SCANCO: $p=0.38$], integration time [K_2HPO_4: $p=0.64$ | HA-SCANCO: $p=0.26$] and projection number [K_2HPO_4: $p=0.86$ | HA-SCANCO: $p=0.77$] did not have any effect on the conversion relationship between μ and ρ_{EQ} for the K_2HPO_4 and HA-SCANCO calibration phantoms (Tables 3 and 4).

Variations in scanning tube voltage and object to X-ray source distance significantly affected the conversion relationship between μ and equivalent mineral densities for K_2HPO_4 and HA-SCANCO calibration phantoms [$p<0.0001$ for all cases]. Higher tube voltage values resulted in reduced attenuation coefficients, with larger reductions in attenuation coefficient values for higher concentration calibration phantoms, and increased attenuation coefficient values as calibration phantoms moved closer to the detector. Additionally, different imaging media, used in conjunction with the liquid K_2HPO_4 calibration phantoms, significantly affected the conversion relationship between μ and equivalent mineral density [$p<0.0001$ for all cases].

The results revealed a highly significant effect of detector size on attenuation coefficient at each concentration level, independent of the effect of projection number. The detector size by concentration term was significant indicating that a higher detection size of 2048×2048 was predictive of a lower mean attenuation although the

Table 3
Linear attenuation coefficients of K_2HPO_4 calibration phantoms scanned under a range of integration time, current, tube voltage, distance from object to X-ray source, detector array size and imaging media settings (standard deviations in parentheses)

		Phantom concentration (g cm^{-3})			
Parameter	Condition	0.050	0.150	0.500	1.000
Integration time (t_{INT})	60ms	1.465 (0.002)	1.968 (0.005)	3.266 (0.008)	4.487 (0.001)
	100ms	1.464 (0.004)	1.970 (0.005)	3.264 (0.004)	4.486 (0.005)
	200ms	1.453 (0.004)	1.956 (0.005)	3.248 (0.006)	4.466 (0.007)
	250ms	1.449 (0.001)	1.953 (0.001)	3.244 (0.002)	4.458 (0.007)
Current (I) $U=45$	88mA	2.215 (0.003)	3.140 (0.002)	5.624 (0.002)	8.089 (0.006)
	177mA	2.226 (0.005)	3.154 (0.006)	5.643 (0.001)	8.101 (0.003)
$U=55$	72mA	1.901 (0.003)	2.654 (0.003)	4.655 (0.003)	6.613 (0.002)
	145mA	1.916 (0.004)	2.673 (0.005)	4.683 (0.002)	6.644 (0.007)
$U=70$	57mA	1.431 (0.004)	1.925 (0.003)	3.202 (0.003)	4.399 (0.005)
	114mA	1.449 (0.001)	1.953 (0.001)	3.244 (0.002)	4.458 (0.007)
Projection number (PN)*	250	1.449 (0.001)	1.953 (0.001)	3.244 (0.002)	4.458 (0.007)
	500	1.448 (0.003)	1.951 (0.005)	3.241 (0.006)	4.453 (0.003)
Tube voltage (U)*	45kVp	2.226 (0.005)	3.154 (0.006)	5.643 (0.001)	8.101 (0.003)
	55kVp	1.916 (0.004)	2.673 (0.005)	4.683 (0.002)	6.644 (0.007)
	70kVp	1.449 (0.001)	1.953 (0.001)	3.244 (0.002)	4.458 (0.007)
Distance from object to X-ray source (D)*	3	1.449 (0.001)	1.953 (0.001)	3.244 (0.002)	4.458 (0.007)
	4	1.468 (0.002)	1.977 (0.005)	3.289 (0.004)	4.520 (0.006)
Detector array size (DET)*	1024^2	1.449 (0.001)	1.953 (0.001)	3.244 (0.002)	4.458 (0.007)
	2048^2	1.335 (0.003)	1.817 (0.004)	3.021 (0.004)	4.136 (0.006)
Media (M)*	Air	1.449 (0.001)	1.953 (0.001)	3.244 (0.002)	4.458 (0.007)
	Saline	1.384 (0.003)	1.810 (0.004)	2.972 (0.006)	4.135 (0.007)
	ETOH	1.401 (0.005)	1.853 (0.005)	3.055 (0.008)	4.250 (.006)

All imaging was performed under a "reference" setting for each parameter with one specific parameter in question being varied. The "reference" setting was $U=70$kVp, $I=I_{HIGH}$ mA, $t_{INT}=250$ms, $D=3$, DET=1024 and M=air. For instance, when studying the effects of current variation, U was maintained at the "reference" 70kVp, t_{INT} at 250ms, D at 3, DET at 1024 and M at air.
*Denotes a parameter with significant effect on attenuation coefficient.

Table 4
Linear attenuation coefficients of HA-SCANCO calibration phantoms scanned under a range of integration time, current, tube voltage distance from object to X-ray source and detector array size settings (standard deviations in parentheses)

		Phantom concentration (g cm^{-3})			
Parameter	Condition	0.099	0.199	0.399	0.800
Integration time (t_{INT})	60ms	1.685 (0.001)	2.357 (0.002)	3.375 (0.004)	5.326 (0.002)
	100ms	1.682 (0.003)	2.359 (0.002)	3.375 (0.006)	5.326 (0.003)
	200ms	1.680 (0.004)	2.354 (0.006)	3.374 (0.007)	5.324 (0.007)
	250ms	1.680 (0.002)	2.353 (0.002)	3.372 (0.003)	5.321 (0.003)
Curent (I) U=45	88mA	2.349 (0.007)	3.471 (0.006)	5.275 (0.028)	8.842 (0.05)
	177mA	2.372 (0.002)	3.509 (0.010)	5.299 (0.008)	8.876 (0.03)
U=55	72mA	1.960 (0.007)	2.830 (0.008)	4.180 (.016)	6.764 (0.031)
	145mA	1.979 (0.001)	2.860 (0.004)	4.199 (0.006)	6.790 (0.006)
U=70	57mA	1.665 (0.003)	2.328 (0.042)	3.357 (0.065)	5.301 (0.103)
	114mA	1.680 (0.002)	2.353 (0.035)	3.372 (0.066)	5.321 (0.106)
Projection number (PN)*	250	1.680 (0.024)	2.353 (0.005)	3.372 (0.002)	5.321 (0.007)
	500	1.685 (0.022)	2.357 (0.002)	3.383 (0.002)	5.327 (0.002)
Tube voltage (U)*	45kVp	2.372 (0.001)	3.509 (0.001)	5.299 (0.001)	8.876 (0.004)
	55kVp	1.979 (0.001)	2.860 (0.003)	4.199 (0.003)	6.790 (0.004)
	70kVp	1.680 (0.001)	2.353 (0.002)	3.372 (0.001)	5.321 (0.002)
Distance from object to X-ray source (D)*	3	1.680 (0.001)	2.353 (0.001)	3.372 (0.001)	5.321 (0.067)
	4	1.867 (0.002)	2.596 (0.001)	3.726 (0.003)	5.888 (0.003)
Detector array size (DET)*	1024^2	1.680 (0.001)	2.353 (0.002)	3.372 (0.002)	5.321 (0.004)
	2048^2	1.652 (0.002)	2.268 (.003)	3.295 (.003)	5.196 (0.004)

Please refer to Table 3 legend for imaging details.
*Denotes a parameter with significant effect on attenuation coefficient.

magnitude of this effect depends on the specific concentration. Simple effects testing revealed a highly significant difference between the 1024×1024 and 2048×2048 detector sizes at each of the five levels of concentration [$p<0.001$ for all cases].

Fig. 5 demonstrates the effects of tube voltage range, object to X-ray source distance and imaging media variations on the linear relationship between X-ray attenuation and equivalent density from K_2HPO_4 calibration phantom, while the effects of object to X-ray source distance and media variations at each tube voltage level are demonstrated in Fig. 5.

A multivariate linear regression approach was used to estimate ρ_{EQ} based on attenuation, tube voltage, object to X-ray source distance, detector size and imaging media for K_2HPO_4 liquid calibration phantoms. This model, explaining 90% of the variation in ρ_{EQ} [$R^2=0.90$, $p<0.001$], was of the form below, where U represents tube voltage in kVp, D represents distance from object to X-ray source in the form of Scanco "diameter" setting (1=33 mm, 2=44 mm, 3=55 mm, 4=82 and 5=99 mm), DET represents detector array size (1024 or 2048), M represents media (1=air, 2=saline, 3=ETOH) and μ represents attenuation coefficient in cm^{-1}.

$$\rho_{EQ} = 14.56 \cdot U - 62.84 \cdot D + 0.70 \cdot \mathrm{DET} - 2.98 \cdot M + 220.70 \cdot \mu - 941.35 \quad (1)$$

Analysis is based on 21 paired measurements from decalcification time points. The ρ_{EQ} of bovine cortical bone samples decalcified over

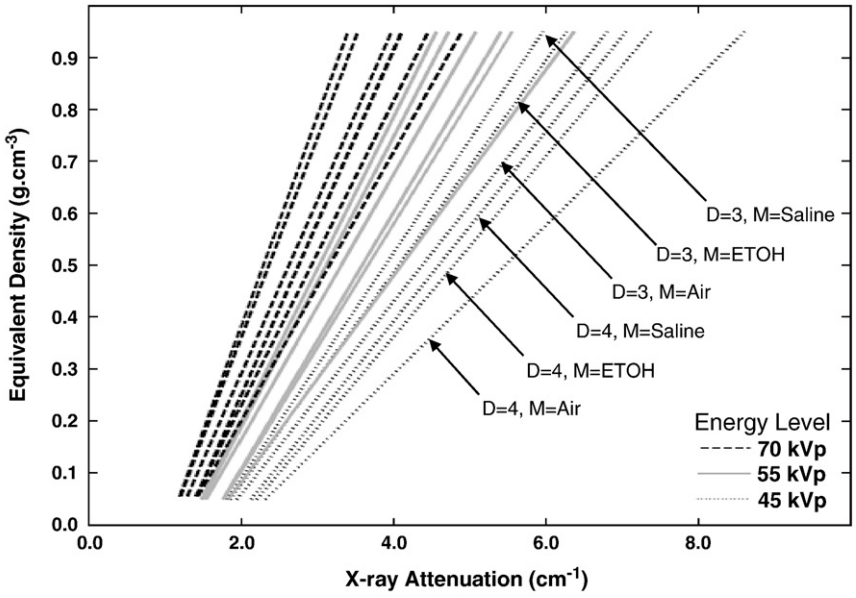

Fig. 5. Equivalent density relationships for 18 configurations of tube voltage (44, 55 and 70 kVp), distance from object to X-ray source ("diameter" settings 3 and 4) and imaging media (air, saline ETOH). The family of dashed lines highlights the distribution of the relationships for tube voltage of 70 kVp and variable D and M settings; whereas, the family of the dashed, solid and dotted lines display the variation observed in the relationships due to changes in the tube voltage.

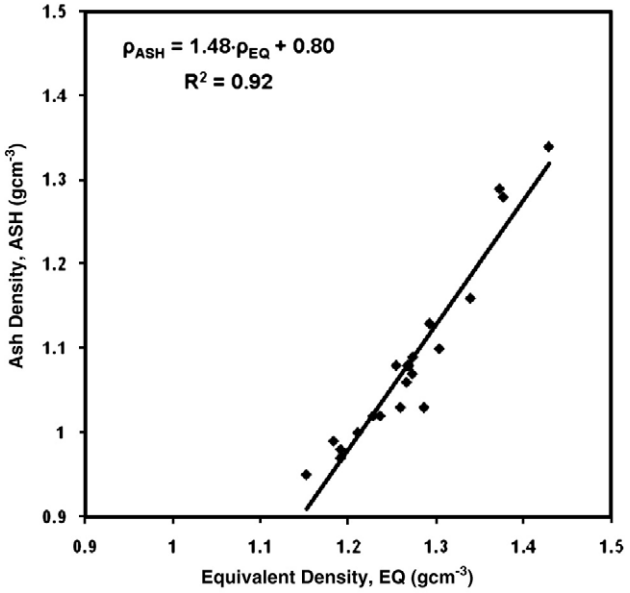

Fig. 6. Correlation of ash and equivalent densities from 21 bovine bone specimens decalcified over a 12-day period.

time points 0, 2, 4, 6, 8, 10 and 12 days (3 specimens per time point) were highly correlated [R^2=0.92] with ash densities of the progressively decalcified samples in this study (Fig. 6). Agreement between equivalent density and ash density was evaluated using a Bland–Altman analysis, where the difference between the two methods of density measurement ($\rho_{EQ} - \rho_{ASH}$), with ash density (ρ_{ASH}) as the reference standard, was plotted against the average density from the two methods (($\rho_{EQ}+\rho_{ASH}$)/2). The average difference was 0.185 g cm^{-3} (solid line) with ±2 SD, 0.095 to 0.275g cm^{-3} (dashed lines), indicating the 95% limits of agreement between the two methods (Fig. 7). The average difference indicates that calibration phantom-based equivalent density tends to be somewhat higher than ash density, on average by 0.185 g cm^{-3}. The limits of agreement indicate that this difference can be as small as 0.095 g cm^{-3} or as large as 0.275 g cm^{-3}. If one were to predict ash density, one could determine the equivalent density and subtract the average value (0.185 g cm^{-3}) as an estimated offset.

Discussion

The distribution of the HA crystals and K_2HPO_4 solutions were homogeneous for both HA-SCANCO and K_2HPO_4 calibration phantoms respectively, therefore, asserting the spatial stability of both calibration phantoms and precluding the need to scan the entire length of each calibration phantom to obtain equivalent densities. Temporal stability is not of much concern for the HA-SCANCO calibration phantoms, as they are made of HA crystals embedded in solid resins, providing the best protection against degradation of calibration phantom materials over time. The temporal stability of the liquid K_2HPO_4 calibration phantoms were studied for a 3-month period, where the calibration phantoms were scanned once a week under identical ambient and imaging conditions and stored away from direct light and heat at all other times (for this study, the HA-SCANCO calibration phantoms were also scanned on a weekly basis as opposed to the regular monthly basis for quality control purpose). This study revealed the stability of K_2HPO_4 calibration phantom over a limited duration of three-months, with less than 0.6% variation from the initial to the end time point for all concentrations. However, any liquid based calibration phantom is susceptible to changes over time via introduction of air bubbles into the calibration phantom through leaching, leakage or both. The relatively long shelf life of the K_2HPO_4 calibration phantom (at least 3-months), its ease of preparation and periodic rescanning as a means of quality control could make this calibration phantom an attractive solution despite the limitations associated with liquid calibration phantoms. However, reproducibility and the ultimate long term stability of these calibration phantoms must be investigated. Moreover, other compounds, such as potassium pyrophosphate, could easily substitute K_2HPO_4 for a variety of calibration phantoms with materials geared towards specific tissue attenuation ranges and needs.

Variations of current and integration time did not affect the attenuation of the calibration phantoms for either the HA-SCANCO or the K_2HPO_4 calibration phantoms. The relationship between the incident and emerging intensities is mostly governed by the energy of the photons, marginalizing the influence of current on the attenuation. As expected, variation of the photon energy levels resulted in significant changes in the attenuation of the calibration phantoms.

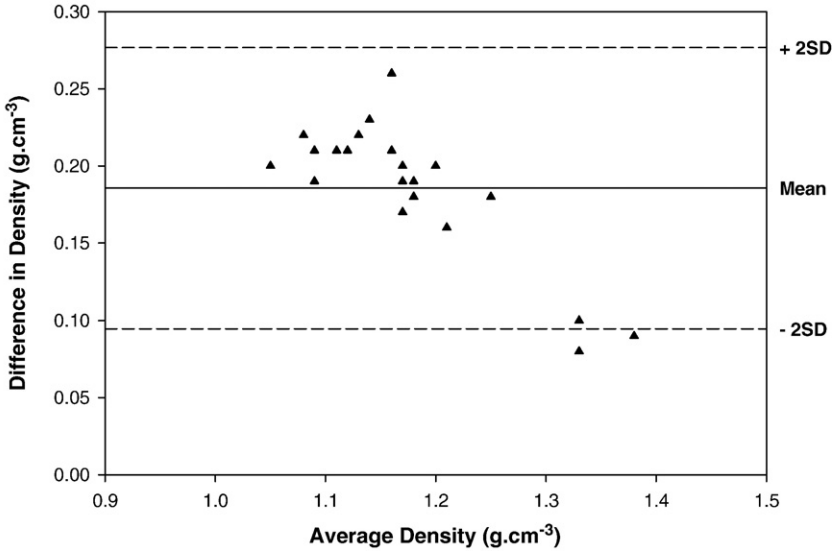

Fig. 7. Bland–Altman plot to evaluate agreement between equivalent and ash density. The difference between the two methods of density measurement ($\rho_{EQ}-\rho_{ASH}$) is plotted against the average density based on the two methods (($\rho_{EQ}+\rho_{ASH}$)/2), where ash density (ρ_{ASH}) is considered the reference standard. The average difference or bias was 0.185 g cm^{-3} (solid line) with ±2 SD, 0.095 to 0.275 g cm^{-3} (dashed lines), indicating the 95% limits of agreement between the two methods.

K_2HPO_4 calibration phantoms demonstrated an average of 16% difference between each tube voltage step (e.g. 45 to 55kVp); whereas the HA-SCANCO calibration phantoms demonstrated on average 19% difference between each tube voltage step. As expected by theory and standards, attenuation is inversely related to the photon energy, with higher tube voltage resulting in lower attenuation. The changes in attenuation remained constant (i.e. the slope and offset of change was constant) across different calibration phantom concentrations (e.g. 0.050, 0.150, 0.500 and 1000 g cm^{-3}) under different photon energy settings, since each material's (K_2HPO_4 or HA) attenuation coefficient is a function of that material's chemical composition, the photon energy and physical density. Scanco Medical initially provided 0.20 g cm^{-3} HA beam hardening correction for cancellous bone surrounded by soft tissue (hence the stipulation placed by Scanco Medical to scan objects surrounded by fluid) in order to use their calibration phantom values to calculate attenuation coefficient and equivalent density. This correction is used by Scanco, for a broad range of scans, to correct the projections of an image to a constant slope. However, this correction factor is not adequate for all ranges of data, and they have recently added 0.70 and 1.20 g cm^{-3} beam hardening corrections to extend the attenuation correction range for intermediate bone surrounded by soft tissue and very dense bone/teeth scanned in air respectively.

Furthermore, moving the object away from the source (increasing D), and closer to the detector, resulted in ~ 10–13% increase in attenuation. This is potentially due to decreased detection of scattered photons as the distance between the object and the detector is reduced (increased detection of scatter results in decreased attenuation, as softer energy scattered beams are detected and the appearance of a more radiolucent material — most photons scattered by incoherent scatter effect are forward peaked and emerge from the material with photon trajectories very similar to the primary beam) [37,38]. Varying the detector array size from 1024×1024 to 2048×2048 resulted in a slight decrease in the attenuation coefficient for both the liquid and solid phantoms as a function of the concentration. This decrease in the attenuation coefficient was ~ 1% for the lowest concentration and 7% for the highest concentration. Regardless of the detector size, the photon flux is the same. Therefore, the relative decrease in the attenuation coefficient for the 2048×2048 detector could be attributed to the number of particles that attenuate the flux being relatively fewer for the higher resolution grid, and greater for the lower resolution grid. This process results in a reduction in the recorded average attenuation of each pixel and concomitantly results in the reduction of the average pixel density reported for the entire cross-section. Additionally, scatter could play an important part in describing this phenomenon, as the energy distribution of photons within a given pixel is more homogeneous if the pixel is smaller. Further investigation of this phenomenon is needed.

Of the advantages of the K_2HPO_4 liquid calibration phantom is its capability to be placed in a variety of media, mimicking different tissue properties (soft tissue, fat) or using different specimen preservation techniques (fresh frozen, saline, formaldehyde, ethyl alcohol, air). This is not possible with the HA-SCANCO calibration phantoms, as the calibration phantom rods are embedded in resin. Different imaging media surrounding the object also affect the attenuation of the K_2HPO_4 calibration phantoms, with saline and ETOH causing larger decreases in calibration phantom attenuation coefficient values. This is partially due to the fact the attenuation of air alone is considered to be zero, therefore little or no photons will be absorbed by air, as opposed to saline or ethyl alcohol which have attenuation larger than zero. Additionally, as the calibration phantom and the imaging media are made of liquid solutions, there is less of an opportunity for inhomogeneities within the calibration phantom and imaging media materials, thereby further reducing the variation in the chemical composition of the calibration phantom and the surrounding tissue.

A multivariate linear regression relationship, capable of explaining 90% of the variation, has been developed in this study to estimate the equivalent density of bone based on the attenuation of the K_2HPO_4 calibration phantom. This model provides a significant improvement in prediction over a linear model containing only μ ($R^2=0.75$) and implies that tube voltage, distance from object to X-ray source, detector array size and imaging media contribute additional independent predictive information with respect to estimating ρ_{EQ}. The single variate linear model is used only to highlight the importance of multiple factors on assessing correct attenuation values in μCT imaging. Inspecting the magnitudes of the *F*-tests would imply that among these four predictors, tube voltage contributes more information than distance from object to X-ray source, detector array size or imaging media with respect to explaining ρ_{EQ}.

The equivalent densities of bovine cortical bone samples decalcified progressively are highly correlated with their ash densities in this study. The Bland–Altman plot revealed very good agreement between equivalent and ash density measurements. The mean difference between the two methods was 19%±3%. A slope test using the Pearson correlation coefficient indicated that the difference between ρ_{EQ} and ρ_{ASH} was constant throughout the range of values for density ($p=0.10$), and the offset difference is due to the fact that mineral density values from two different methods are compared to one another. While ashing is the gold standard for such measures, equivalent mineral density measured from μCT imaging is highly correlated to the gold standard with the offset being partially due to the fact that the liquid calibration phantom material is K_2HPO_4 and not HA. In practice, one could adjust for the bias by calculating equivalent density and subtracting a translation constant equal to 0.2 g cm^{-3}. This is possible since the Bland–Altman analysis indicated only an offset difference between the ash and equivalent density values and no change in the slope of the curve over the density range. This correction is not a beam-hardening correction, rather a linear offset correction between measurements of equivalent bone density via μCT versus the gold standard of ashing. As this equation was derived using specimens from this study, it cannot be used on the same specimens to assess improvement over currently obtained attenuation/density values. Therefore, this equation will be used in future studies to independently assess its density improvement contribution.

These findings indicate that the relationship used to convert linear X-ray attenuation coefficient measured by μCT to an equivalent bone mineral density for K_2HPO_4 and HA-SCANCO calibration phantoms are significantly influenced by the tube voltage level, object to X-ray source distance, detector array size and imaging media. Therefore, any time one of these scanning parameters is changed, the appropriate calibration file for that setting will be used to properly derive the bone mineral tissue density from the X-ray attenuation coefficient. If the proper conversion relationship, using these calibration phantoms, is then generated, the equivalent bone mineral density can be accurately specified.

Both HA-SCANCO solid and K_2HPO_4 liquid calibration phantoms can be used to assess equivalent bone density. However, different imaging media cannot be used with solid calibration phantoms, but they provide stability over time, not matched by their liquid counterparts. The K_2HPO_4 liquid calibration phantoms provide a cost effective, easy to prepare, stable and convenient means to perform quantitative μCT analysis using any μCT system, with the ability to choose different imaging media according to study needs. Liquid calibration phantoms in general are susceptible to leakage and/or leaching, however, the current calibration phantom was shown to be leak and bubble free for at least three months. The current study was validated using cortical bones only, and the results might not correlate with low density and/or trabecular bone specimens. Also, a Scanco system was used in this study. Further work can be performed on μCT imaging systems manufactured by other companies.

In conclusion, this study provides an in-depth analysis of the use of calibration phantoms to measure equivalent bone mineral density in high resolution μCT imaging. Particularly, it investigated two calibration phantoms, one available commercially with the scanner and the other

manufactured by the authors, to report and model the effects of varying imaging parameters on measurement of equivalent bone mineral density in hopes of offering the scientific community basic guidelines in the rapidly growing yet vastly understudied use of μCT imaging to assess bone mineral density. The importance of this work is to highlight the factors that affect the assessment of bone tissue density from micro-computed tomography in general, and not to provide a comparative assessment of bone tissue density assessment from different manufacturers, as they all use very similar sources and detectors. The HA-SCANCO solid and K_2HPO_4 liquid calibration phantoms proved to be useful each with specific positive and negative characteristics. As μCT based assessment of bone mineral density is and will be on the rise in future, it is recommended to establish guidelines and standards in order to accurately compare these density measures across laboratories and scanner makes and models worldwide. For now, the best way to obtain accurate attenuation values from μCT imaging is to include appropriately sized calibration phantoms with each specimen to be imaged. The presence of calibration phantoms in each specimen cross-sectional image can provide a direct conversion to known density values.

Acknowledgments

Financial support for this project was provided by a Fulbright Full Grant for Graduate Study and Research Abroad and the Swiss National Science Foundation (R.M.; Grant PP-104317/1). The authors would like to acknowledge the members of the OBL at Beth Israel Deaconess Medical Center and the Bioelectronics group at University and ETH Zürich, specifically Dr. Robert Fajardo (OBL), John Muller (OBL), Philipp Schneider (ETH) and Rhiannon Evison (ETH) for their help and support with this project. Additionally, the authors would like to acknowledge the insightful comments made by the reviewers. Their comments were directly incorporated into the manuscript.

References

[1] Dempster DW, Cosman F, Kurland ES, Zhou H, Nieves J, Woelfert L, et al. Effects of daily treatment with parathyroid hormone on bone microarchitecture and turnover in patients with osteoporosis: a paired biopsy study. J Bone Miner Res 2001;16:1846–53.
[2] von Stechow D, Balto K, Stashenko P, Muller R. Three-dimensional quantitation of periradicular bone destruction by micro-computed tomography. J Endod 2003;29:252–6.
[3] Braillon PM, Salle BL, Brunet J, Glorieux FH, Delmas PD, Meunier PJ. Dual energy X-ray absorptiometry measurement of bone mineral content in newborns: validation of the technique. Pediatr Res 1992;32:77–80.
[4] Panattoni GL, Sciolla A, Isaia GC. Densitometric study of developing vertebral bodies. Calcif Tissue Int 1995;57:74–7.
[5] Panattoni GL, D'Amelio P, Di Stefano M, Sciolla A, Isaia GC. Densitometric study of developing femur. Calcif Tissue Int 1999;64:133–6.
[6] Salle BL, Braillon P, Glorieux FH, Brunet J, Cavero E, Meunier PJ. Lumbar bone mineral content measured by dual energy X-ray absorptiometry in newborns and infants. Acta Paediatr 1992;81:953–8.
[7] Braillon PM, Lapillonne A, Ho PS, Bouvier R, Bochu M, Salle BL. Assessment of the bone mineral density in the lumbar vertebrae of newborns by quantitative computed tomography. Skeletal Radiol 1996;25:711–5.
[8] Roschger P, Grabner BM, Rinnerthaler S, Tesch W, Kneissel M, Berzlanovich A, et al. Structural development of the mineralized tissue in the human L4 vertebral body. J Struct Biol 2001;136:126–36.
[9] Skedros JG, Bloebaum RD, Bachus KN, Boyce TM, Constantz B. Influence of mineral content and composition on graylevels in backscattered electron images of bone. J Biomed Mater Res 1993;27:57–64.
[10] Skedros JG, Bloebaum RD, Bachus KN, Boyce TM. The meaning of graylevels in backscattered electron images of bone. J Biomed Mater Res 1993;27:47–56.
[11] Ito M. Assessment of bone quality using micro-computed tomography (micro-CT) and synchrotron micro-CT. J Bone Miner Metab 2005;23:115–21 Suppl.
[12] Homolka P, Nowotny R. Production of phantom materials using polymer powder sintering under vacuum. Phys Med Biol 2002;47:N47–52.
[13] Homolka P, Gahleitner A, Prokop M, Nowotny R. Optimization of the composition of phantom materials for computed tomography. Phys Med Biol 2002;47:2907–16.
[14] D'Souza WD, Madsen EL, Unal O, Vigen KK, Frank GR, Thomadsen BR. Tissue mimicking materials for a multi-imaging modality prostate phantom. Med Phys 2001;28:688–700.
[15] Zerhouni EA, Spivey JF, Morgan RH, Leo FP, Stitik FP, Siegelman SS. Factors influencing quantitative CT measurements of solitary pulmonary nodules. J Comput Assist Tomogr 1982;6:1075–87.
[16] Jones FA, Wiedemann HP, O'Donovan PB, Stoller JK. Computerized tomographic densitometry of the solitary pulmonary nodule using a nodule phantom. Chest 1989;96:779–83.
[17] Byng JW, Mainprize JG, Yaffe MJ. X-ray characterization of breast phantom materials. Phys Med Biol 1998;43:1367–77.
[18] Rumberger JA, Brundage BH, Rader DJ, Kondos G. Electron beam computed tomographic coronary calcium scanning: a review and guidelines for use in asymptomatic persons. Mayo Clin Proc 1999;74:243–52.
[19] Braillon PM. Quantitative computed tomography precision and accuracy for long-term follow-up of bone mineral density measurements: a five year in vitro assessment. J Clin Densitom 2002;5:259–66.
[20] Chen X, Lam YM. Technical note: CT determination of the mineral density of dry bone specimens using the dipotassium phosphate phantom. Am J Phys Anthropol 1997;103:557–60.
[21] Faulkner KG, Gluer CC, Estilo M, Genant HK. Cross-calibration of DXA equipment: upgrading from a Hologic QDR 1000/W to a QDR 2000. Calcif Tissue Int 1993;52:79–84.
[22] Goodsitt MM, Rosenthal DI. Quantitative computed tomography scanning for measurement of bone and bone marrow fat content. A comparison of single- and dual-energy techniques using a solid synthetic phantom. Invest Radiol 1987;22:799–810.
[23] Goodsitt MM, Kilcoyne RF, Gutcheck RA, Richardson ML, Rosenthal DI. Effect of collagen on bone mineral analysis with CT. Radiology 1988;167:787–91.
[24] Goodsitt MM, Christodoulou EG, Larson SC, Kazerooni EA. Assessment of calibration methods for estimating bone mineral densities in trauma patients with quantitative CT: an anthropomorphic phantom study. Acad Radiol 2001;8:822–34.
[25] Goodsitt MM. Conversion relations for quantitative CT bone mineral densities measured with solid and liquid calibration standards. Bone Miner 1992;19:145–58.
[26] Kalender WA, Klotz E, Suess C. Vertebral bone mineral analysis: an integrated approach with CT. Radiology 1987;164:419–23.
[27] Witt MR, Cameron JR. An improved bone standard containing dipotassium hydrogen phosphate solution for the intercomparison of different bone scanning systems. Washington, DC: US Atomic Energy Commission; 1970.
[28] Cann CE, Genant HK. Precise measurement of vertebral mineral content using computed tomography. J Comput Assist Tomogr 1980;4:493–500.
[29] Cann CE. Quantitative CT for determination of bone mineral density: a review. Radiology 1988;166:509–22.
[30] Kalender WA, Felsenberg D, Genant HK, Fischer M, Dequeker J, Reeve J. The European Spine Phantom—a tool for standardization and quality control in spinal bone mineral measurements by DXA and QCT. Eur J Radiol 1995;20:83–92.
[31] Ruegsegger P, Kalender WA. A phantom for standardization and quality-control in peripheral bone measurements by Pqct and Dxa. Phys Med Biol 1993;38:1963–70.
[32] Nuzzo S, Meneghini C, Braillon P, Bouveir R, Mobilio S, Peyrin F. Microarchitectural and physical changes during fetal growth in human vertebral bone. J Bone Miner Res 2003;18:760–8.
[33] Sanada S, Kawahara K, Yamamoto T, Takashima T. New tissue substitutes representing cortical bone and adipose tissue in quantitative radiology. Phys Med Biol 1999;44:N107–12.
[34] Ruegsegger P, Koller B, Müller R. A microtomographic system for the nondestructive evaluation of bone architecture. Calcif Tissue Int 1996;58:24–9.
[35] Montgomery DC. Design and Analysis of Experiments. 5th ed. New York: John Wiley; 2001.
[36] Vittinghoff E, Glidden DV, Shiboski SC, McCulloch CE. Regression methods in biostatistics. Linear. logistic, survival, and repeated measures models. New York: Springer; 2005.
[37] Ter-Pogossian MM. Basic principles of computed axial tomography. Semin Nucl Med 1977;7:109–27.
[38] Glover GH. Compton scatter effects in CT reconstructions. Med Phys 1982;9:860–7.